ORIGINAL PAPER

Optimized preparation of $LiNi_{0.6}Mn_{0.2}Co_{0.2}O_2$ with single crystal morphology cathode material for lithium-ion batteries

Bing Huang [1,2] · Meng Wang [3] · Xiangwu Zhang [2] · Guodong Xu [1] · Yijie Gu [4]

Abstract

Single crystal $LiNi_{0.6}Mn_{0.2}Co_{0.2}O_2$ cathode materials with excellent electrochemical properties were synthesized by adjusting the calcination, ball milling, and reheating procedures. The results showed that the particle size of single crystal material obtained by the optimization method was 1.2–4.4 μm. And the material exhibited a superior discharge capacity of 190.1 mAh g^{-1} with high capacity retention of 96.0% after 50 cycles at 1.0 C. And the material had a discharge capacity of 162.6 mAh g^{-1} at 5.0 C with the capacity retention of 83.0% compared with its capacity at 0.1 C. The diffusion coefficient of lithium ions in the single crystal material reached to 10^{-13} cm^2 s^{-1} after 50 cycles. By proper reheating process, the particle morphology was optimized to form a smooth particle surface, and the lattice arrangement was more orderly, which was conductive to improving electrochemical performance of the material.

Keywords Single crystal morphology · Primary particles · Cathode material · Lithium-ion diffusion · Lithium-ion batteries

Introduction

In recent years, with the continuous improvement of preparation and modification technology for $LiNi_xMn_yCo_{1-x-y}O_2$ cathode materials, the materials have become the mainstream of cathode materials applied in lithium-ion batteries [1–3]. At present, due to the limitation of synthesis method, the conventional morphology of $LiNi_xMn_yCo_{1-x-y}O_2$ cathode materials shows generally secondary particles formed by primary particle agglomeration, rather than primary single crystal morphology which is similar to $LiCoO_2$ [4, 5]. This agglomeration of primary particles causes the compaction density of $LiNi_xMn_yCo_{1-x-y}O_2$ (about 3.3 g cm^{-3}) which is much lower

than that of $LiCoO_2$ (about 4.0 g cm^{-3}), which results in a low volume energy density of the battery. In addition, the secondary particles tend to crush when the electrodes are rolled, which will affect electrochemical performance of the cathode materials.

Preparing single crystal primary particles is an effective method to solve the above defects. There are many advantages of single crystal cathode materials [6, 7]. For instance, high compaction density is not easily crushed when rolled into electrodes and can be mixed with $LiCoO_2$ without affecting its compaction density. In view of these, some research institutes and enterprises actively explore some effective methods for preparing single crystal primary particles of $LiNi_xMn_yCo_{1-x-y}O_2$ [8]. However, the preparation process of single crystal primary particles of $LiNi_xMn_yCo_{1-x-y}O_2$ is complex, because the commonly used crystal crushing process often leads to deterioration of electrochemical properties. At the same time, single crystal materials also have some shortcoming, such as low rate performance which caused by large micron-sized particles. All these factors make it difficult to prepare single crystal materials with excellent electrochemical performance. Therefore, there are few reports on the successful preparation of $LiNi_xMn_yCo_{1-x-y}O_2$ single crystal particles.

Based on the above analysis, it is urgent to develop a facile and effective method to produce $LiNi_xMn_yCo_{1-x-y}O_2$ with single crystal primary particles and excellent electrochemical properties. In this study, the effects of calcination, ball milling,

✉ Meng Wang
manyou2005@163.com

✉ Yijie Gu
guyijie@sdust.edu.cn

1 Institute of New Energy on Chemical Storage and Power Sources, Yancheng Teachers University, Yancheng 224000, China

2 Wilson College of Textiles, North Carolina State University, Raleigh, NC 27695-8301, USA

3 China Academy of Machinery Science and Technology Group Co. Ltd., Beijing 100044, China

4 School of Mechanical-Electronic and Vehicle Engineering, Weifang University, Weifang 261061, China

Fig. 1 FESEM images of (A) $Ni_{0.6}Mn_{0.2}Co_{0.2}(OH)_2$ and (B) after preheated at 700 °C
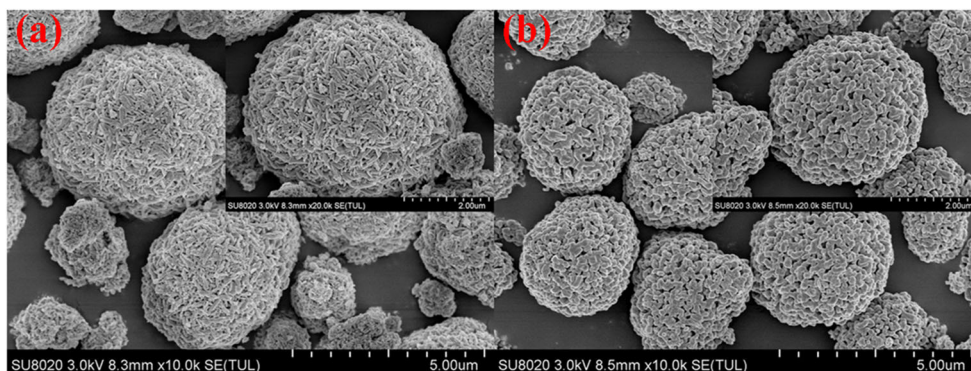
and reheating processes on the formation of single crystal primary particles are studied in detail. The coexistence of single crystal morphology and excellent electrochemical properties are realized in $LiNi_{0.6}Mn_{0.2}Co_{0.2}O_2$ by controlling the calcination, ball milling, and reheating processes. The products have the following characteristics: suitable single crystal particle size provides short path for lithium ions, smooth crystal surface facilitates the material's full contact with electrolyte and conductive agent, and more orderly lattice arrangement for lithium ions easily transport.

Experimental

Material synthesis

The $Ni_{0.6}Mn_{0.2}Co_{0.2}(OH)_2$ precursor was conventional commercial materials, which purchased from Ningbo Jinhe New materials Co., Ltd. Li_2CO_3 was produced by Sinopharm Chemical Reagent Co., Ltd. The precursor was heated from 25 to 700 °C at a speed of 5 °C min^{-1} (the subsequent heating rate in this paper was the same), and then calcination was kept at 700 °C for 5 h. After that, the obtained materials were mixed with Li_2CO_3 in a molar ratio of Li: M (the sum of transition metal ions) = 1.05:1 (the excess lithium salt was used to compensate for evaporation during high-temperature calcination) and was annealed at different calcination conditions to obtain $LiNi_{0.6}Mn_{0.2}Co_{0.2}O_2$, 900 °C for 20 h (the obtained sample named as a-1), 900 °C for 8 h (named as b-1), 900 °C for 8 h then 960 °C for 3 h (named as c-1), 900 °C for 8 h then 960 °C for 5 h (named as d-1), 900 °C for 5 h then 960 °C for 3 h (named as e-1), and 900 °C for 5 h then 960 °C for 5 h (named as f-1). To crush the agglomerated samples, the obtained a-1, b-1, c-1, d-1, e-1, and f-1 were ball milled at 500 r min^{-1} for 1 h, and they were named as a-2, b-2, c-2, d-2, e-2, and f-2, respectively. To smooth the surface morphology and improve electrochemical performance, the ball-milled materials were reheated at 940 °C for 5 h, which were named as a-3, b-3, c-3, d-3, e-3, and f-3, respectively.

Material characterizations

X-ray diffraction (XRD) patterns of the samples were performed on a Rigaku Ultima IV-185 (Cu K_α radiation) between 10 and 80° 2θ at a scan rate of 8° min^{-1}. The morphology of materials was observed by a FEI Quanta 250 field emission

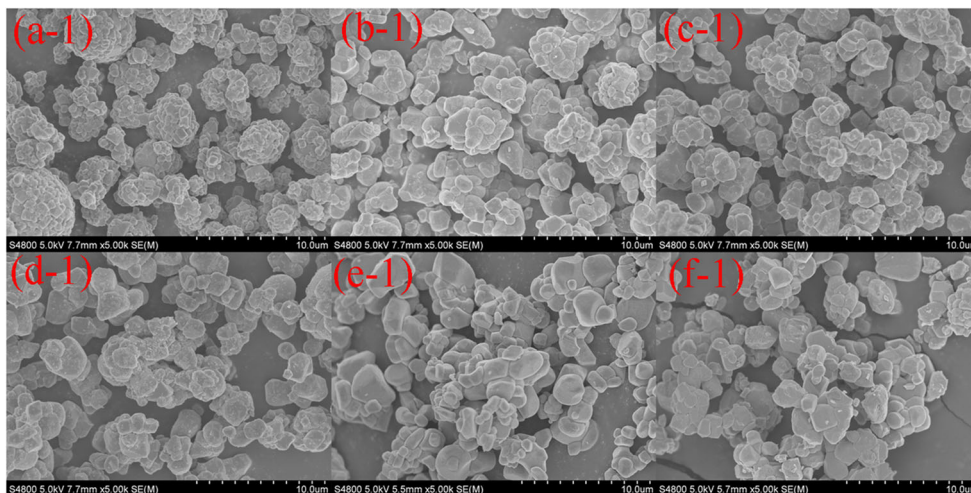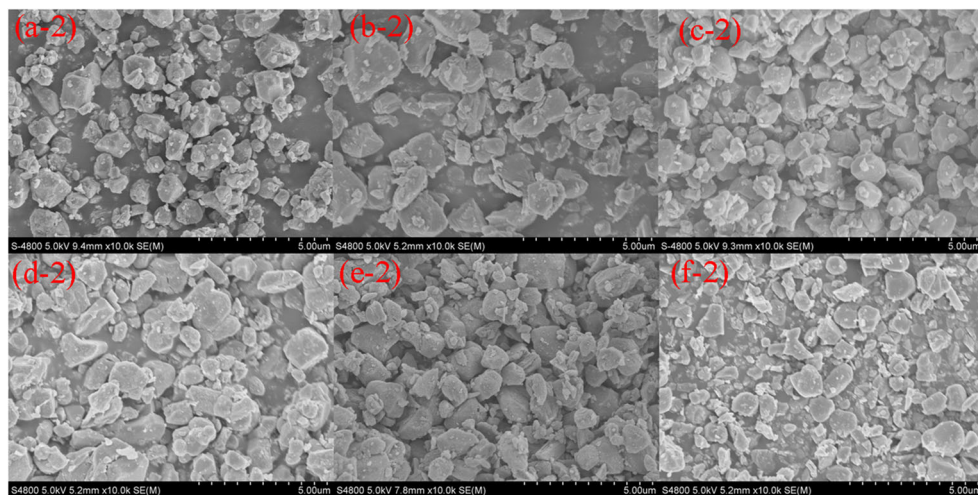Fig. 2 FESEM images of the a-1, b-1, c-1, d-1, e-1, and f-1 samples

Fig. 3 FESEM images of the a-2, b-2, c-2, d-2, e-2, and f-2 samples

scanning electron microscope (FESEM) on a HORIBA EMAX instrument. In order to observe the micro-structure of the material, high-resolution transmission electron microscopy (HRTEM) images and selected area electron diffraction (SAED) patterns were applied on a JEM2100. The particle size distribution was carried out by a laser particle size analyzer (Mastersizer 2000).

Electrochemical measurements

The electrochemical performances of the materials were tested using CR2025 type coin cells. The cathode electrodes were prepared by casting a mixture containing 85 wt% active materials, 10 wt% acetylene black, and 5 wt% polyvinylidene fluoride on Al current collector foil. The counter electrode was lithium metal foil, the separator was Celgard 2400 film, and the electrolyte was 1 M $LiPF_6$ in ethylene carbonate (EC)-dimethyl carbonate (DMC) (1:1, v/v). Electrochemical measurements were performed at 0.1 C (1.0 C = 200 mA g^{-1})

between 2.8 and 4.5 V on Land CT2001A. The electrochemical impedance spectroscopy (EIS) measurements were carried out using a CHI604D impedance analyzer, with an amplitude voltage of 5 mV and the frequency range of 10^{-2}–10^5 Hz.

Results and discussion

Morphology and structural analysis

Figure 1 presents FESEM images of $Ni_{0.6}Mn_{0.2}Co_{0.2}(OH)_2$ precursor before and after preheating at 700 °C. The precursor exhibits a spherical structure assembled of closely packed small needle shaped primary grains. After preheating, the spherical particle size becomes smaller with more gap between primary grains, and the needle primary particles become polyhedral particles. Figure 2 shows FESEM of a-1, b-1, c-1, d-1, e-1, and f-1 samples. All of them are secondary

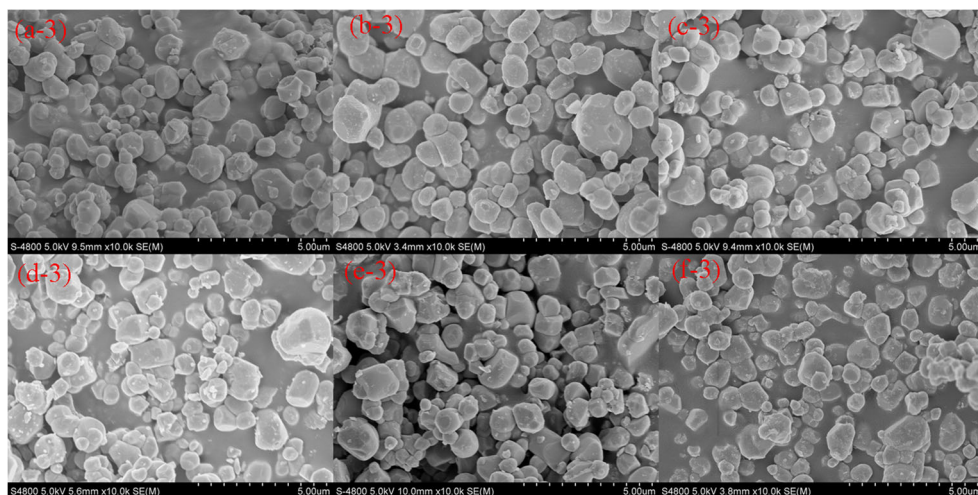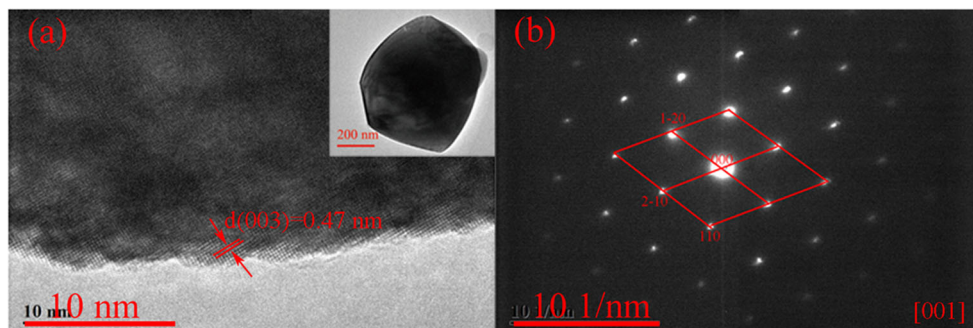**Fig. 4** FESEM images of the a-3, b-3, c-3, d-3, e-3, and f-3 samples

Fig. 5 (A) HRTEM images and (B) SAED pattern of e-3

particle agglomerates. The agglomeration degree of a-1 is the most serious with the largest particle size of 2–7 μm. This is because the material calcined at high temperature for a long time leads to an increase in particle size and serious agglomeration [9]. For the other samples, especially d-1, e-1, and f-1, the secondary particle size is small and the agglomeration is weakened. This is due to their relatively short calcination time, which inhibits the growth of particles.

To crush the agglomerated materials, the obtained a-1, b-1, c-1, d-1, e-1, and f-1 samples were ball milled at 500 r min^{-1} for 1 h to obtain a-2, b-2, c-2, d-2, e-2, and f-2 samples, and their FESEM images are presented in Fig. 3. It can be found that all the agglomerated particles disperse into single primary particles after ball milled. However, the particle size is uneven and there are many fine particles on the surface of the samples, which can be due to the pulverization force during ball milling. Such non-smooth surface will increase the contact area between the material and electrolyte, which will cause more side reactions and lead to the attenuation of electrochemical performance [10, 11]. Besides that, the hexagonal layered structure of materials can be damaged by ball milling, which is reflected by the comparing XRD of e-1, e-2, and e-3. The poor electrochemical performance of a-2, b-2, c-2, d-2, e-2,

and f-2 samples will be proved by the following electrochemical performance section.

Since high-temperature treatment can reshape the particle surface morphology and stabilize the crystal structure, it is considered to optimize the surface and crystal structure of the material by reheating [12]. The above a-2, b-2, c-2, d-2, e-2, and f-2 samples are reheated at 940 °C for 5 h to obtain the samples a-3, b-3, c-3, d-3, e-3, and f-3, and the morphology is presented in Fig. 4. As compared in Fig. 3, it is found that all the samples have more obvious single crystal primary morphology after reheating, and the most obvious change is that all the particles have very smooth surface morphology. The tap density of single crystal e-3 is 2.7 g cm^{-3}, which is improved when compared with e-1 (2.3 g cm^{-3}). The particle size distribution of e-1 and e-3 was carried out to show the particle difference of the agglomerated and single crystal samples. e-1 displays a large particle size distribution of 3.7–13.7 μm, with D50 at around 7.3 μm. On the contrary, e-3 shows a homogeneous microsphere size distribution with a small particle size of 1.2–4.4 μm, and D50 is around 2.3 μm. It is reported that a small particle size shortens the lithium-ion migration path, which is conductive to improving rate performance of cathode materials [13]. Therefore, it can be deduced that e-3 has excellent rate performance, which will be proved in the later rate test. e-3 is also investigated by HRTEM and SAED to accurately prove that the sample is single crystal and the results are shown in Fig. 5. From HRTEM, the sample shows distinct lattice fringes and d-spacing of the (003) plane is 0.47 nm, while SAED patterns
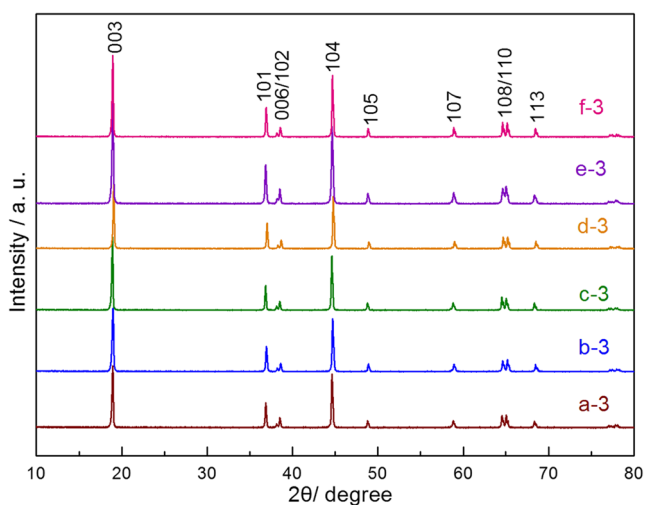

Fig. 6 XRD patterns of a-3, b-3, c-3, d-3, e-3, and f-3 samples

Table 1 Lattice parameters of the a-3, b-3, c-3, d-3, e-3, and f-3

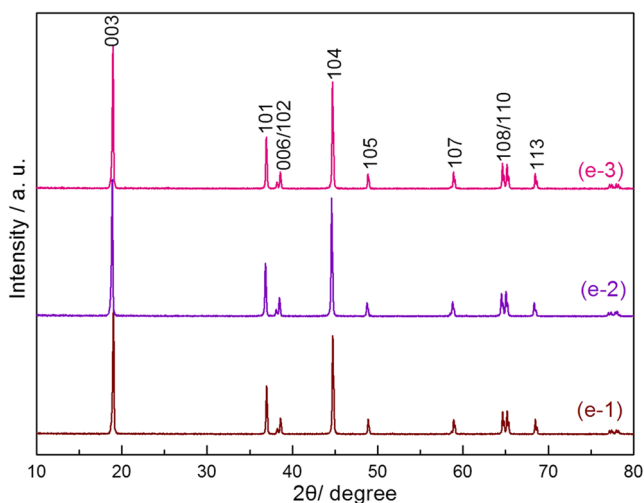| Samples	a (Å)	c (Å)	c/a	$I_{(003)}/I_{(104)}$
a-3	2.8660	14.0550	4.9040	1.1506
b-3	2.8688	14.0313	4.8910	1.2023
c-3	2.8660	14.0792	4.9127	1.3168
d-3	2.8640	14.0528	4.9067	1.2229
e-3	2.8664	14.0823	4.9129	1.3294
f-3	2.8658	14.0733	4.9108	1.2496

Fig. 7 XRD patterns of e-1, e-2, and e-3 samples

for the [001] zone axis show a set of well-defined spots accurately confirm that e-3 particles consist of perfect single crystals [14, 15].

In order to analyze the structure of a-3, b-3, c-3, d-3, e-3, and f-3 samples, XRD data of them are presented in Fig. 6. Obviously, all the samples have hexagonal α-$NaFeO_2$ structure with $R3m$ space group. The (006)/(102) and (108)/(110) peaks are significantly splitted, which suggests all the materials possess highly ordered layered structure [16]. For Li^+ and Ni^{2+} having similar ion radius, Ni^{2+} can easily insert into the Li slab from the Ni site, which is called cation mixing. The $I_{(003)}/I_{(104)}$ reflects the degree of cation mixing in the layered hexagonal structure and the higher value of $I_{(003)}/I_{(104)}$, the lower cation mixing is [17]. In general, $I_{(003)}/I_{(104)} < 1.2$ means that undesirable cation mixing takes place [18]. Except for sample a-3, $I_{(003)}/I_{(104)}$ of other samples are higher than 1.2, which imply the materials have excellent layered structure. Among these samples, e-3 has the highest $I_{(003)}/I_{(104)}$ of 1.3294, which indicates it presents the best electrochemical performance. For the sample a-3, the $I_{(003)}/I_{(104)}$ is only 1.1506, which is related to the long calcination time at high temperature. Jade 6.0 software is used to calculate lattice parameters a and c, and the results are shown in Table 1. Parameter a represents interlayer metal-metal distance, while parameter c stands for the sum of the slab thickness and the interslab space thickness [19]. The large c is generally

associated with fast Li-ion insertion/extraction [20–22]. The e-3 sample possesses the largest parameter c/a value which indicates that the lattice of e-3 has the priority to grow along the c-axis and thus to promote emigration of lithium ions. Besides that, a well-defined hexagonal layered structure is also strongly related to c/a; a higher c/a ratio presents a better-ordered layered hexagonal structure [14]. In general, a well-defined hexagonal layered structure is also strongly related to c/a, and a higher c/a ratio presents a better-ordered layered hexagonal structure [23–25]. The c/a is greater than 4.9 indicating that the synthesized cathode materials have a better hexagonal structure with lower cation mixing [26, 27]. The e-3 sample possesses the largest c/a value which indicates that the material has the best hexagonal structure with the lowest cation mixing [27]. In order to further analyze the crystal structure changes of the materials before and after reheating, Fig. 7 is added to present the XRD of e-1, e-2, and e-3, and the lattice parameters are shown in Table 2. Obviously, the hexagonal layered structure of e-2 is seriously damaged by ball milling, which reflects by the lowest values of c/a and $I_{(003)}/I_{(104)}$. After reheating treatment, these parameters which reflect the degree of ordered layered hexagonal structure have been greatly improved for e-3. Therefore, reheating treatment can make the lattice arrangement of materials more orderly and lower cation mixing degree, which is favorable for lithium-ion migration and electrochemical performance.

Electrochemical discussion

Figure 8 A illustrates the initial charge and discharge voltage profiles of a-1, b-1, c-1, d-1, e-1, and f-1 samples at 0.1 C, and Fig. 8B shows the cycling performance and coulombic efficiency of the samples at 1.0 C. All the samples have a typical potential plateau at about 3.75 V and deliver discharge capacity over 180.0 mAh g^{-1} at 0.1 C. For example, a-1, b-1, c-1, d-1, e-1, and f-1 deliver 200.1, 180.6, 179.6, 185.0, 183.9, and 187.2 mAh g^{-1} at 0.1 C, respectively. Although, sample a-1 shows the largest discharge capacity, the cycling performance at 1.0 C is not superior, which decreases from 177.3 mAh g^{-1} at the 1st cycle to 148.8 mAh g^{-1} at the 50th cycle, with the capacity retention of 83.9%. On the contrary, e-1 shows the highest discharge capacity retention of 94.2% after 50 cycles, and it still has 166.6 mAh g^{-1} at the 50th cycle. The difference in capacity retention of samples depends on the difference in the calcination process

The initial charge/discharge curves at 0.1 C and cycling performance (coulombic efficiency) at 1.0 C of the ball-milled materials are shown in Fig. 9. Obviously, the discharge capacity and cycling performance are significantly reduced after ball milling. Take e-2 for instance, it is obtained by ball milling of e-1. Before ball milling, the material (e-1) delivers 176.8 mAh g^{-1} at 1.0 C with the capacity retention of 94.2%

Table 2 Lattice parameters of the e-1, e-2, and e-3

Samples	a (Å)	c (Å)	c/a	$I_{(003)}/I_{(104)}$
e-1	2.8621	14.0533	4.9101	1.2088
e-2	2.8660	14.0503	4.9021	1.1552
e-3	2.8664	14.0823	4.9129	1.3294

Fig. 8 (A) Initial charge/
discharge voltage profiles at 0.1
C; (B) cycling performance and
coulombic efficiency at 1.0 C for
a-1, b-1, c-1, d-1, e-1, and f-1
samples
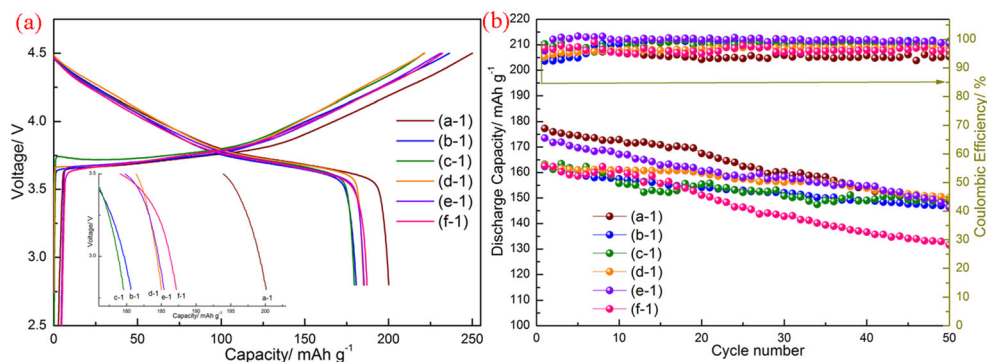
after 50 cycles. However, it shows a greatly damaged cyclic performance after ball milling. The discharge capacity of e-2 at the 36th cycle is only 137 mAh g^{-1}, which is 84.2% of that at the 1st cycle. It can be seen that although ball milling can effectively produce cathode material particles with single crystal morphology, it also has side effects to cause a sharply decline of electrochemical performance. One main reason is the crystal structure gets some damage due to the intense ball milling process, which will be proved in the following XRD test. Besides that, lithium oxide reside in the LiNi$_{0.6}$Mn$_{0.2}$Co$_{0.2}$O$_2$ can react with CO$_2$ and trace amount of water molecules in the air to form Li$_2$CO$_3$ and LiOH during the ball milling process [28, 29]. These impurities exist on the surface of cathode material will hinder the Li$^+$-ion diffusion during the charge and discharge process for their insulation, leading to deterioration of electrochemical performance for they can cause side reactions with electrolyte [30, 31]. Therefore, we need to explore how to overcome the side effects caused by the ball milling process.

Reheating method is considered to optimize the material surface and crystal structure for it can reshape the micro-morphology of the material surface and stabilize the crystal structure [28]. Figure 10 shows the first charge/discharge curves at 0.1 C and cycle performance curves at 1.0 C of the reheated materials. Compared with Fig. 9, the initial discharge capacity of the samples are significantly improved after reheating. The initial discharge capacities of a-3, b-3, c-3, d-

3, e-3, and f-3 samples are 181.9, 180.4, 184.4, 186.8, 190.1, and 191.8 mAh g^{-1}, respectively. Besides that, the cycling performance of the samples is also greatly enhanced after reheating and the capacity retention rates of all the samples are increased to 90.6–96.0%. Take e-3 for example, the first discharge capacity at 1.0 C is 180.7 mAh g^{-1}, and it gently decreases to 173.5 mAh g^{-1} after 50 cycles with the capacity retention rate of 96.0%. The remarkable improvement of electrochemical properties after reheating is largely attributed to the improvement of particle surface smoothness and the reduction of side reactions between material and electrolyte. FESEM of the e-1 and e-3 electrodes after 50 cycles are presented in Fig. 11 to further prove the advantages of single crystal primary particle morphology. Obviously, there are much more fine particles on the surface of e-1 than on e-3, which are caused by side reactions between the cathode material and electrolyte. This may be due to the non-smooth surface of e-1 which caused by the agglomerated particles increasing the contact area between the material and the aggregated particles often forming inter-granular cracks after excessive cycling, which aggravates the inter-facial side reactions and causes the degradation of the electrical properties [32].

The discharge capacities and capacity retention of a-3, b-3, c-3, d-3, e-3, and f-3 samples at different current densities are displayed in Fig. 12. The batteries are charged at 0.1 C and then discharged at various C rates for 5 cycles, respectively.

Fig. 9 (A) Initial charge/
discharge voltage profiles at 0.1
C; (B) cycling performance and
coulombic efficiency at 1.0 C of
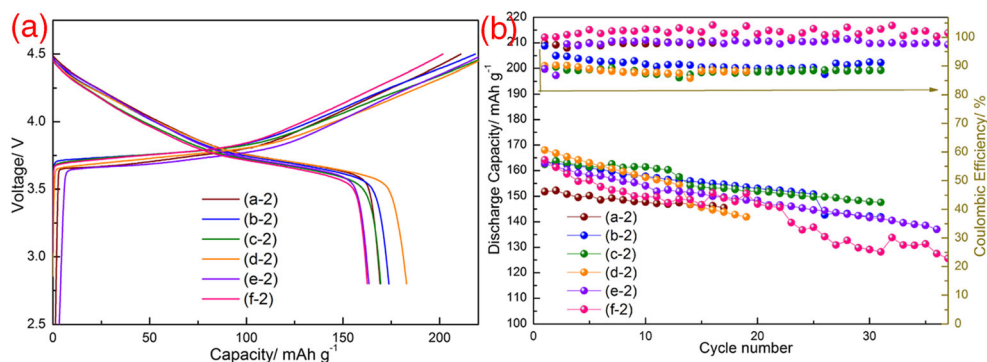a-2, b-2, c-2, d-2, e-2, and f-2
samples

Fig. 10 (A) Initial charge/ discharge voltage profiles at 0.1 C; (B) cycling performance and coulombic efficiency at 1.0 C of a-3, b-3, c-3, d-3, e-3, and f-3 samples
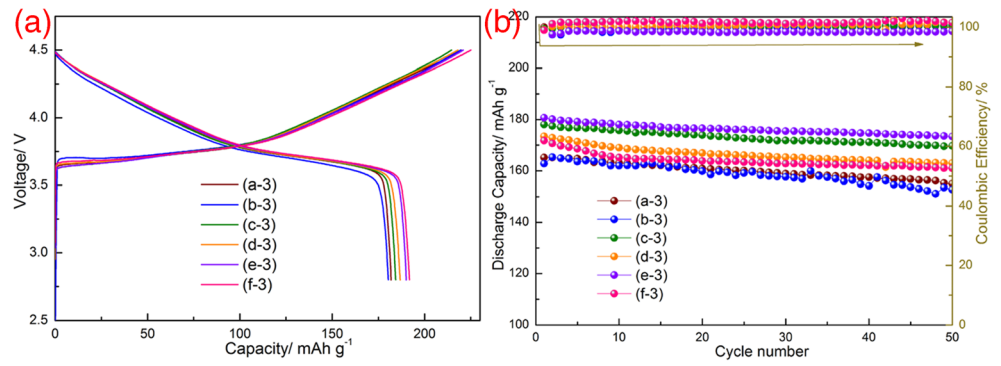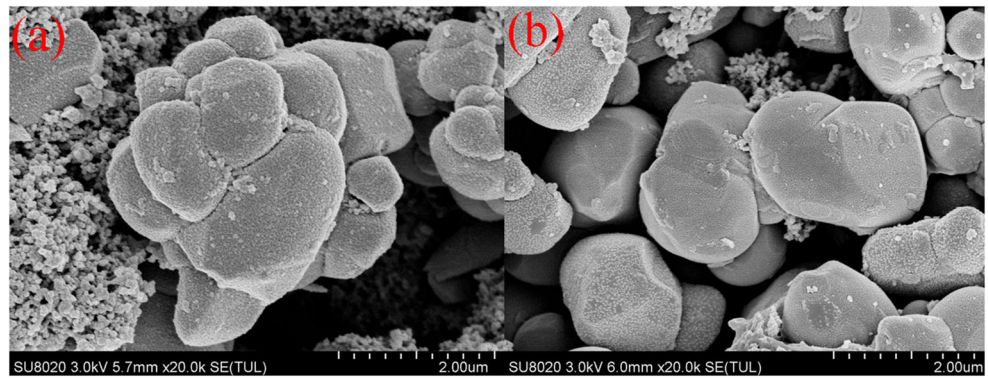

Fig. 11 FESEM of (a) e-1 and (b) e-3 after 50 cycles

Fig. 12 (A) Discharge capability and (B) capability retention at different current rates of a-3, b-3, c-3, d-3, e-3, and f-3 samples
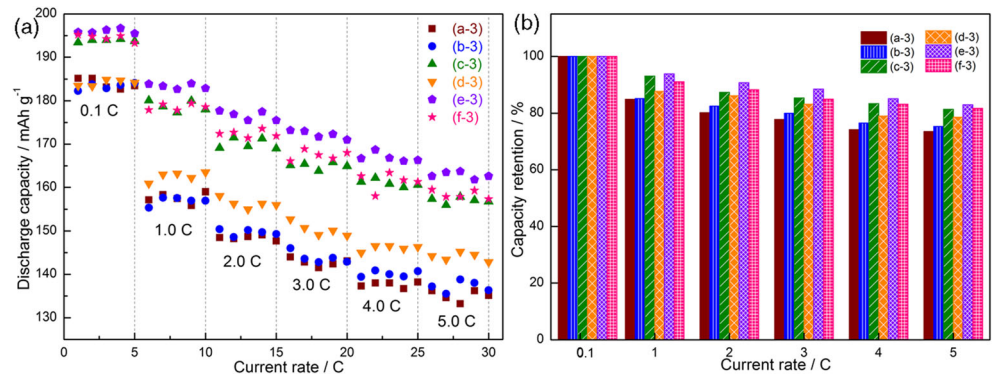

Fig. 13 EIS plots of the a-3, b-3, c-3, d-3, e-3, and f-3 samples at 4.3 V
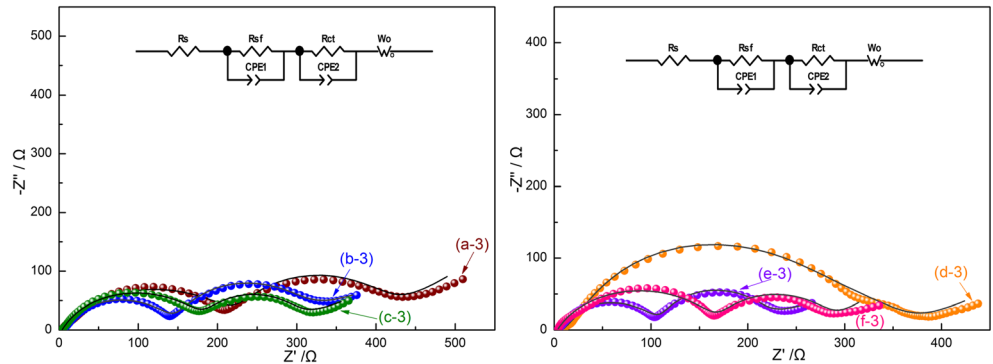
Table 3 Fitting values of the electrochemical impedance of a-3, b-3, c-3, d-3, e-3, and f-3 samples

Sample	R_s (Ω)	R_{sf} (Ω)	R_{ct} (Ω)	$R_{sf} + R_{ct}$ (Ω)
a-3	3.7	222.2	163.6	385.8
b-3	4.5	124.5	122.9	247.4
c-3	3.4	172.5	95.4	267.9
d-3	8.4	150.8	203.0	353.8
e-3	2.5	93.1	82.9	176.0
f-3	3.3	166.1	107.4	273.5

As shown in Fig. 12, discharge capacities of all the samples decrease gradually with the increases of discharge rate; these phenomena are caused by the internal polarization of lithium intercalation and deintercalation reaction at high currents [33]. Compared with other samples, e-3 presents distinct improved rate capacity. When the discharge rate amplified to 3.0 C, the discharge capacity of e-3 is the highest among the samples which reaches to 173.2 mAh g^{-1}. And the capacity retention is 88.5% when compared with the discharge capacity at 0.1 C. By contrast, a-3, b-3, c-3, d-3, and f-3 samples exhibits discharge capacities of 144.0, 146.0, 165.1, 152.7, and 166.1 mAh g^{-1} at 3.0 C, which are 77.8, 80.0, 85.4, 83.2, and 85.0% of the discharge capacity at 0.1 C, respectively. With the further increases of discharge current rate to 5.0 C, the excellent rate performance of e-3 is more obvious. The e-3 possesses the highest discharge capacity of 162.6 mAh g^{-1} at 5.0 C, which is 83.0% of its discharge capacity at 0.1 C. In comparison, a-3 delivers the lowest discharge capacity of 136.2 mAh g^{-1} at 5.0 C, which is only 73.5% of its discharge capacity at 0.1 C. The enhanced rate capacity of e-3 is mainly attributed to the well-formed layered structure and the largest c lattice parameter value. Minor cation (Li$^+$/Ni^{2+}) mixing in the layered cathode materials indicates few Ni^{2+} in the Li layer, which is beneficial to lithium-ion migration and result in high discharge capacity at high discharge rate. Furthermore, the single crystal particle size is small (D50 is around 2.3 μm), which can provide short paths for lithium-ion intercalation and deintercalation. For a-3, it has lower c lattice parameter value

and high cation mixing degree which deteriorates its rate performance.

Electrochemical impedance spectroscopy (EIS) is a very useful technique to study kinetic processes of lithium-ion intercalation and deintercalation in the electrode. Electrochemical impedance spectroscopy (EIS) of a-3, b-3, c-3, d-3, e-3, and f-3 samples after 50 cycles at charged state of 4.3 V is presented in Fig. 13. The points represent experimental data, and dark solid lines are data calculated by Zview2 software. Generally, the high-frequency semicircle is related to the impedance of Li$^+$-ion migration through the inter-facial layer between electrode and electrolyte (R_{sf}), while the semicircle in the medium frequency stands for the impedance of charge transfer at the interface between electrolyte and electrode (R_{ct}). The low frequency line is ascribed to the solid-state diffusion of lithium ions in the positive electrode (W_o) [34]. An equivalent electrical circuit is inserted in Fig. 13. R_s represents solution resistance of the cell, while CEP2 and CEP1 reflect the non-ideal capacitance of surface layer and double-layer, respectively. The resistance values obtained by Zview2 are listed in Table 3. R_{sf} and R_{ct} of e-3 is the lowest, which represents migration of Li$^+$ ions through the SEI film is the easiest and indicates small charge transfer resistance through the interface between electrolyte and electrode. It can be seen from Table 3 that a-3 has the largest $R_{sf} + R_{ct}$ of 385.8 Ω, while e-3 has the lowest $R_{sf} + R_{ct}$ of 176.0 Ω. Because the rate performance of the material highly depends on the charge transfer process, it is demonstrated that e-3 has the best rate performance among the samples. This is consistent with the previous electrochemical test performance.

As analyzed in the EIS section, the migration of lithium ions within the materials phase is reflected in the straight sloping line at low frequency region in the impedance spectrum. As a result, the diffusion coefficient of lithium ions (D_{Li^+}) can be obtained by the slope of the straight line in the low frequency region by the following formula [35, 36]:

$$D_{Li} = \frac{R^2 T^2}{2n^4 F^4 A^2 C_{Li^+}^2 \sigma^2} \tag{1}$$

Fig. 14 (A) the profiles of $Z^{'}$ vs. $\omega^{-1/2}$ and (B) the corresponding D_{Li^+} obtained from the EIS data of a-3, b-3, c-3, d-3, e-3, and f-3 samples
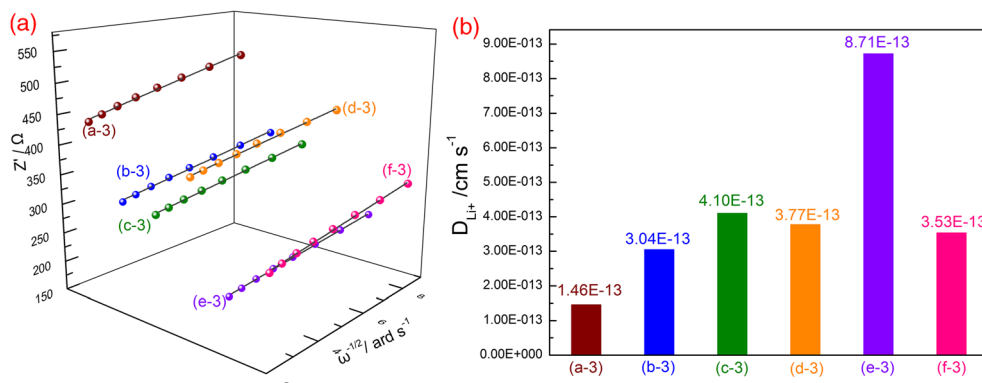
In the formula, n is the number of electrons per molecule during electrochemical reaction process, F represents the Faraday constant, A refers to the active surface area of the electrochemical reaction (here is surface area of the electrode), C_{Li^+} is the concentration of lithium ions in the materials, R is the gas constant, T is the absolute temperature, and σ stands for the Warburg factor which can be calculated by the following formula:

$$Z' = R_s + R_{ct} + \sigma\omega^{-1/2} \qquad (2)$$

Z', R_s, R_{ct}, and ω stand for the real part of impedance, electrolyte resistance, charge transfer resistance, and angular frequency, respectively. The linear relationship of Z' and $\omega^{-1/2}$ is shown in Fig. 14(A). The σ value can be obtained by the slope of the fitted straight line. According to formulas (1) and (2), D_{Li^+} can be calculated and compared in Fig. 14(B). The e-3 processes the highest D_{Li^+} of 8.71×10^{-13} cm^2 s^{-1}, while a-3 is only 1.46×10^{-13} cm^2 s^{-1}. The raised D_{Li^+} presents lithium ions migrate more smoothly in e-3 than in other samples, which is consistent with the improved rate capability. This can be due to its large parameter c value, which promotes migration of lithium ions. Besides that, excellent hexagonal structure with low cation mixing also promotes migration of lithium ions.

Conclusion

The excellent $LiNi_{0.6}Mn_{0.2}Co_{0.2}O_2$ cathode materials with single crystal primary particle morphology have been synthesized by adjusting the calcination and reheating procedure. The results show that different calcination procedures have great influence on the electrochemical properties of the products, but the morphology of single crystal particles is closely related to ball milling and reheating processes. Ball milling can effectively disperse secondary agglomerated particles into primary dispersed single crystal particles, but the surface of the formed particles is not smooth and hexagonal layered structure is damaged, which can greatly reduce the electrochemical properties of the materials. The reheating process can optimize the material morphology to form the smooth surface and to form excellent hexagonal structure with low cation mixing. Ball milling and reheating processes are combined to produce the smooth primary single crystal particles with perfect cycling performance and rate capability. The e-3 sample exhibits the highest discharge capacity, the best cyclability and the most excellent rate capability. Lithium-ion transport is relatively easy within the single crystal material, and the diffusion coefficient of lithium ions after 50 cycles in the single crystal material can reach 10^{-13} cm^2 s^{-1}. This study presents an effective, simple, and convenient method to prepare the single crystal primary $LiNi_xMn_yCo_{1-x-y}O_2$ particles with excellent electrochemical properties.

References

1. Yang H, Wu HH, Ge M, Li L, Yuan Y, Yao Q, Chen J, Xia L, Zheng J, Chen Z, Duan J, Kisslinger K, Zeng XC, Lee WK, Zhang Q, Lu J (2019) Simultaneously dual modification of Ni-rich layered oxide cathode for high-energy lithium-ion batteries. Adv Funct Mater 29: 1808825–1808837
2. Becker D, Borner B, Nolle R, Diehl M, Klein S, Rodehorst U, Schmuch R, Winter M, Placke T (2019) Surface modification of Ni-rich $LiNi_{0.8}Co_{0.1}Mn_{0.1}O_2$ cathode material by tungsten oxide coating for improved electrochemical performance in lithium-ion batteries. ACS Appl Mater Interfaces 5:18404–18414
3. Qiu L, Xiang W, Tian W, Xu C, Li YC, Wu ZG, Chen TR, Jia K, Wang D, He FR, Guo XD (2019) Polyanion and cation co-doping stabilized Ni-rich Ni-Co-Al material as cathode with enhanced electrochemical performance for Li-ion battery. Nano Energy 63: 103818–103826
4. Ryu WH, Lim SJ, Kim WK, Kwon HS (2014) 3-D dumbbell-like $LiNi_{1/3}Mn_{1/3}Co_{1/3}O_2$ cathode materials assembled with nano-building blocks for lithium-ion batteries. J Power Sources 257: 186–191
5. Manthiram A, Song B, Li W (2017) A perspective on nickel-rich layered oxide cathodes for lithium-ion batteries. Energy Storage Mater 6:125–139
6. Wang L, Wu B, Mu D, Liu X, Peng Y, Xu H, Gai L, Wu F (2016) Single-crystal $LiNi_{0.6}Co_{0.2}Mn_{0.2}O_2$ as high performance cathode materials for Li-ion batteries. J Alloys Compd 674:360–367
7. Zhao N, Chen J, Liu ZQ, Ban KJ, Duan WJ (2018) Porous $LiNi_{1/3}Co_{1/3}Mn_{1/3}O_2$ microsheets assembled with single crystal nanoparticles as cathode materials for lithium ion. J Alloy Compd 768:782–788
8. Zeng X, Zhu J, Yang L, Zhou L, Shao L, Hu S, Huang C, Yang C, Qian D, Xi X (2019) Electrochemical stabilities of surface aluminum-doped $LiNi_{0.5}Co_{0.2}Mn_{0.3}O_2$ single crystals under different cutoff voltages. J Electroanal Chem 838:94–100
9. Xu Z, Xiao L, Wang F, Wu K, Zhao L, Li MR, Zhang HL, Wu Q, Wang J (2014) Effects of precursor, synthesis time and synthesis temperature on the physical and electrochemical properties of $Li(Ni_{1-x-y}Co_xMn_y)O_2$ cathode materials. J Power Sources 248: 180–189
10. Geder J, Hoster HE, Jossen A, Garche J, Yu DYW (2014) Impact of active material surface area on thermal stability of $LiCoO_2$ cathode. J Power Sources 257:286–292
11. Zhu X, Li X, Zhu Y, Jin S, Wang Y, Qian Y (2014) Porous $LiNi_{0.5}Mn_{1.5}O_4$ microspheres with different pore conditions: preparation and application as cathode materials for lithium-ion batteries. J Power Sources 261:93–100
12. Yi TF, Wang Y, Xue J, Meng J, Yue CB, Zhu RS (2011) Effect of treated temperature on structure and performance of $LiCoO_2$ coated by $Li_4Ti_5O_{12}$. Surf Coat Technol 205:3885–3889
13. Nara H, Morita K, Mukoyama D, Yokashima T, Momma T, Osaka T (2017) Impedance analysis of $LiNi_{1/3}Mn_{1/3}Co_{1/3}O_2$ cathodes with different secondary-particle size distribution in lithium-ion battery. Electrochim Acta 241:323–330

14. Zheng Z, Guo XD, Chou SL, Hua WB, Liu HK, Dou SX, Yang XS (2016) Uniform Ni-rich LiNi$_{0.6}$Co$_{0.2}$Mn$_{0.2}$O$_2$ porous microspheres: facile designed synthesis and their improved electrochemical performance. Electrochim Acta 191:401–410

15. Huang B, Wang M, Zuo Y, Zhao Z, Zhang X, Gu Y (2020) The effects of reheating process on the electrochemical properties of single crystal LiNi$_{0.6}$Mn$_{0.2}$Co$_{0.2}$O$_2$. Solid State Ionics 345: 115200–115208

16. Jiang X, Sha Y, Cai R, Shao Z (2015) The solid-state chelation synthesis of LiNi$_{1/3}$Co$_{1/3}$Mn$_{1/3}$O$_2$ as a cathode material for lithium-ion batteries. J Mater Chem A 3:10536–10544

17. Lee SH, Lee S, Jin BS, Kim HS (2019) Preparation and electrochemical performance of Ni-rich LiNi$_{0.91}$Co$_{0.06}$Mn$_{0.03}$O$_2$ cathode for high-energy LIBs. Int J Hydrog Energy 44:13684–13689

18. Li N, An R, Su Y, Wu F, Bao L, Chen L, Zheng Y, Shou H, Chen S (2013) The role of yttrium content in improving electrochemical performance of layered lithium-rich cathode materials for Li-ion batteries. J Mater Chem A 1:9760–9767

19. Fu C, Li G, Luo D, Li Q, Fan J, Li L (2014) Nickel-rich layered microspheres cathodes: lithium/nickel disordering and electrochemical performance. ACS Appl Mater Interfaces 6:15822–15831

20. Huang Z, Wang Z, Jing Q, Guo H, Li X, Yang Z (2016) Investigation on the effect of Na doping on structure and Li-ion kinetics of layered LiNi$_{0.6}$Co$_{0.2}$Mn$_{0.2}$O$_2$ cathode material. Electrochim Acta 192:120–126

21. Qu Y, Mo Y, Jia X, Zhang L, Du B, Lu Y, Li D, Chen Y (2019) Flux growth and enhanced electrochemical properties of LiNi$_{0.5}$Co$_{0.2}$Mn$_{0.3}$O$_2$ cathode material by excess lithium carbonate for lithium-ion batteries. J Alloy Compd 788:810–818

22. Yi TF, Han X, Chen B, Zhu YR, Xie Y (2017) Porous sphere-like LiNi$_{0.5}$Mn$_{1.5}$O$_4$-CeO$_2$ composite with high cycling stability as cathode material for lithium-ion battery. J Alloy Compd 703:103–113

23. Yang J, Hou M, Haller S, Mang Y, Wang C, Xia Y (2016) Improving the cycling performance of the layered Ni-rich oxide cathode by introducing low-content Li$_2$MnO$_3$. Electrochim Acta 189:101–110

24. Yuan J, Wen J, Zhang J, Chen D, Zhang D (2017) Influence of calcination atmosphere on structure and electrochemical behavior of LiNi$_{0.6}$Co$_{0.2}$Mn$_{0.2}$O$_2$ cathode material for lithium-ion batteries. Electrochim Acta 230:116–122

25. Zhang JT, Tan XH, Guo LM, Jiang Y, Liu SN, Wang HF, Kang XH, Chu WG (2019) Controllable formation of lithium carbonate surface phase during synthesis of nickel-rich LiNi$_{0.9}$Mn$_{0.1}$O$_2$ in air and its protection role in electrochemical reaction. J Alloy Compd 771: 42–50

26. Dong S, Zhou Y, Hai C, Zeng J, Sun Y, Shen Y, Li X, Ren X, Qi G, Zhang X, Ma L (2019) Ultrathin CeO$_2$ coating for improved cycling and rate performance of Ni-rich layered LiNi$_{0.7}$Co$_{0.2}$Mn$_{0.1}$O$_2$ cathode materials. Ceram Int 45:144–152

27. Zhang X, Chen Z, Schwarz B, Sigel F, Ehrenberg H, An K, Zhang Z, Zhang Q, Li Y, Li J (2017) Kinetic characteristics up to 4.8 V of layered LiNi$_{1/3}$Co$_{1/3}$Mn$_{1/3}$O$_2$ cathode materials for high voltage lithium-ion batteries. Electrochim Acta 227:152–161

28. Jo JH, Jo CH, Yashiro H, Kim SJ, Myung ST (2016) Re-heating effect of Ni-rich cathode material on structure and electrochemical properties. J Power Sources 313:1–8

29. Cho DH, Jo CH, Cho W, Kim YJ, Yashiro H, Sun YK, Myung ST (2014) Effect of residual lithium compounds on layer Ni-rich Li[Ni$_{0.7}$Mn$_{0.3}$]O$_2$. J Electrochem Soc 161:A920–A926

30. Visbal H, Fujiki S, Aihara Y, Watanabe T, Park Y, Doo S (2016) The influence of the carbonate species on LiNi$_{0.8}$Co$_{0.15}$Al$_{0.05}$O$_2$ surface for all-solid-state lithium ion battery performance. J Power Sources 269:396–402

31. Ding Y, Deng B, Wang H, Li X, Chen T, Yan X, Wan Q, Qu M, Peng G (2019) Improved electrochemical performances of LiNi$_{0.6}$Co$_{0.2}$Mn$_{0.2}$O$_2$ cathode material by reducing lithium residues with the coating of Prussian blue. J Alloy Compd 774:451–460

32. Kim J, Lee H, Cha H, Yoon M, Park M, Cho J (2018) Prospect and reality of Ni-rich cathode for commercialization. Adv Energy Mater 8:1702028–1702053

33. Zhang XL, Cheng FY, Zhang K, Liang YL, Yang SQ, Liang J, Chen J (2012) Facile polymer-assisted synthesis of LiNi$_{0.5}$Mn$_{0.5}$O$_4$ with a hierarchical micro-nanostructure and high rate capability. RSC Adv 2:5669–5675

34. He W, Yuan DD, Qian JF, Ai XP, Yang HX, Cao YL (2013) Enhanced high-rate capability and cycling stability of Na-stabilized layered Li$_{1.2}$[Co$_{0.13}$Ni$_{0.13}$Mn$_{0.54}$]O$_2$ cathode material. J Mater Chem A 1:11397–11403

35. Li L, Chen Z, Zhang Q, Xu M, Zhou X, Zhu H, Zhang K (2015) A hydrolysis-hydrothermal route for the synthesis of ultrathin LiAlO$_2$-inlaid LiNi$_{0.5}$Co$_{0.2}$Mn$_{0.3}$O$_2$ as a high-performance cathode material for lithium ion batteries. J Mater Chem A 3:894–904

36. Wang M, Gong Y, Gu Y, Chen Y, Chen L, Shi H (2019) Effects of fast lithium-ion conductive coating layer on the nickel rich layered oxide cathode material. Ceram Int 45:3177–3185